Multi-physics modelling of 3D-printed concrete evolution in environmental conditions

Alice Gribonval, Maxime Pierre, Nicolas Ducoulombier, Karam Sab, Romain Mesnil, Jérémy Bleyer

Cement and Concrete Research 196 (2025) 107918

Contents lists available at ScienceDirect

Cement and Concrete Research

journal homepage: www.elsevier.com/locate/cemconres

Multi-physics modelling of 3D-printed concrete evolution in environmental conditions

Alice Gribonval [a,b,*], Maxime Pierre [b], Nicolas Ducoulombier [a], Karam Sab [b], Romain Mesnil [b], Jérémy Bleyer [b]

[a] XtreeE, 18 rue du Jura, Rungis, 94150, France
[b] Laboratoire Navier, École nationale des ponts et chaussées, Univ. Gustave Eiffel, CNRS, Champs-sur-Marne, France

ARTICLE INFO

Keywords:
3D concrete printing
Multi-physics modelling
Thermo-poro-mechanical model
Compressive strength
Plastic shrinkage

ABSTRACT

Extrusion-based 3D-printed cementitious structures have high water loss after printing provoking significant plastic shrinkage. In this study, we propose a thermo-poro-mechanical model of printed cementitious materials, driven by the experimental observation of a positive correlation between the printed wall thickness and compressive strength at the hardened state. The model is developed to represent evaporation at free surfaces, water consumption associated to the cement hydration and water flow within the material, accounting for their effect on temperature variations, strains and on the evolution of stiffness and compressive strength. Comparisons of compressive strength and plastic shrinkage with experiments are presented, demonstrating the validity of the proposed model. In the absence of protective measures, wall thickness is positively correlated with compressive strength and negatively correlated with shrinkage. When preventing evaporation by putting printed specimens in water, plastic shrinkage is significantly reduced and the compressive strength is increased, reaching similar values as cast samples.

1. Introduction

3D concrete printing (3DCP) is a construction technique which consists in the layer-by-layer deposition of a concrete filament along a predefined path to obtain the desired geometry. The automation of the construction process with 3D printing allows for an increased geometric freedom [1,2] at reduced cost [3–5] and a better quality control. Its use in the construction industry has expanded rapidly in the previous years, although it remains limited due to several challenges.

The absence of reinforcement in most printed structures [6] and the lack of relevant standards [6–9] are impeding the development of this technology. Additionally, the high evaporation due to the absence of formwork and the lack of curing measures causes significant plastic shrinkage [10–14] from early age. Few studies also mention that effects of evaporation are also visible at the hardened state, causing a significant decrease in compressive strength compared to samples for which evaporation is restricted due to a limited and incomplete cement hydration [15–17].

Plastic shrinkage and plastic shrinkage cracking of 3D printed structures have been studied experimentally [10–12] and several models have been proposed [13,14] to predict plastic shrinkage. However, there are only few studies on the effects of environmental conditions on mechanical properties at the hardened state, most of such studies focusing on potential anisotropy [17–20], cold joints at the interface between layers [1,21,22] and reinforcement methods [23–25].

Nevertheless, Wang et al. [15] proposed a model to estimate the compressive strength of a concrete specimen considering both cement hydration and drying due to evaporation, showing an influence of the wall thickness on the compressive strength. However, their model needs extensive calibration and is not suited for high strength concrete sometimes used in 3DCP. Besides, the compressive strength is directly estimated from the degree of hydration without modelling any internal stresses and strains. Ma et al. [16] showed experimentally that printed specimens exposed to the ambient air have a lower compressive and flexural strength than specimens cured in a humid environment. However, no model was proposed to simulate the compressive strength obtained in given curing conditions, and the influence of the wall thickness on the compressive strength was not studied.

Coupled models have already been developed, often to model the early-age behaviour of mortars or concrete. Ulm and Coussy [26] modelled the material considering thermo-chemo-mechanical couplings. Other authors have completed their approach by specifically considering the porous aspect of the material [27,28]. The aim of the article

* Corresponding author at: Laboratoire Navier, École nationale des ponts et chaussées, Univ. Gustave Eiffel, CNRS, Champs-sur-Marne, France.
E-mail addresses: alice.gribonval@enpc.fr, alice.gribonval@xtreee.com (A. Gribonval).

https://doi.org/10.1016/j.cemconres.2025.107918
Received 16 January 2025; Received in revised form 11 April 2025; Accepted 28 April 2025
Available online 14 May 2025

is to leverage recent advances in coupled physics modelling to provide guidance on the influence of curing conditions on shrinkage and compressive strength of 3D-printed structures at the hardened state.

In the present study, we first show experimentally that the compressive strength of printed samples is positively correlated to the wall thickness, and that curing the printed samples in water suppresses the decrease of compressive strength. A thermo-poro-mechanical model is then proposed to represent the effects of hydration and drying on the mechanical properties of the printed material, depending on the environmental conditions. Eventually, the influence of the wall thickness and of the curing conditions on plastic shrinkage is studied both experimentally and numerically.

The present study focuses on a 2K system, that is a printing system for which an activator is added to the mix right before extrusion to enhance buildability [29]. However, the presented model can easily be applied to 1K systems for which all components of the printing mix are added together.

The manuscript is organised as follows: Section 2 presents the compressive strength results. The model theoretical framework and experimental calibration are described in Section 3 and Section 4 respectively. Eventually, results and validation are exposed in Section 5 and discussed in Section 6.

2. Influence of the wall thickness and the curing conditions on the compressive strength

The compressive strength of the material was measured on printed samples in order to assess the influence of the wall thickness and of the curing conditions on the compressive strength measured at 20 days.

2.1. Materials and methods

2.1.1. Printing mix

The printing mix was prepared with Holcim Tector 3D mix 849 (formerly 3DPG and NAG3 [30]) with a maximum aggregate size of 1 mm and a water-to-powder ratio of 0.1. Between $20\,\mathrm{mL\,L^{-1}}$ and $24\,\mathrm{mL\,L^{-1}}$ of activator were added to the mix during printing. Specimens were printed with XtreeE's printing head mounted on a 6-axis robotic arm, with a 20 mm circular nozzle. Specimens were printed with a constant flow rate of $1\,\mathrm{L\,min^{-1}}$, the robot speed varying from $41\,\mathrm{mm\,s^{-1}}$ to $84\,\mathrm{mm\,s^{-1}}$ depending on the wall thickness.

2.1.2. Compressive strength measurements

Hollow cylinders were printed with a constant filament height of 9 mm, a constant average diameter of 127 mm, a total height of 260 mm and three different wall thicknesses: 24 mm (size S), 35 mm (size M) and 48 mm (size L), as illustrated on Fig. 1. For a cured reference, specimens with the same dimensions as specimens M were also printed in water (specimens C). Each specimen size was printed three times, and the compressive strength of a given specimen size was estimated based on the average value of the three measurements. All specimens are visible on Fig. 2. Cast specimens were also poured in $11 \times 22\,\mathrm{cm}$ cylindrical moulds. When removed from the moulds two days after casting, those specimens were kept in water containers until the compressive strength measurements.

The printed specimens were stored in ambient conditions for 20 days after printing. For comparison, specimens that were printed in water were kept in a water container until the compression tests. The upper and lower surfaces of the cylinders were cut to remove the first and last layers which were uneven due to boundary effects, and smooth contact surfaces were then prepared. The internal and external diameters, height and weight of all specimens were measured before the compressive strength measurements.

The compressive strength was measured 20 days after printing with a hydraulic press with a capacity of 3000 kN. The loading speed was set to $10\,\mathrm{kN\,s^{-1}}$, which corresponds to $0.6\,\mathrm{MPa\,s^{-1}}$ to $1.1\,\mathrm{MPa\,s^{-1}}$ depending on the wall thickness. For each specimen, the maximum applied force is reported to estimate the compressive strength of the specimen.

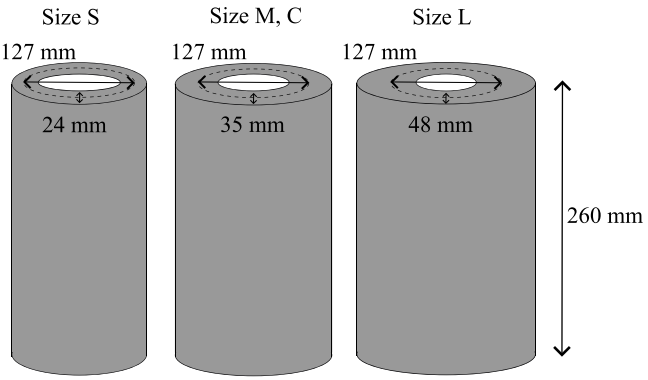

Fig. 1. Dimensions of the printed specimens for compressive strength measurements.

Since the specimens' lateral surfaces are not smooth due to the layer-by-layer deposition, the estimation of the reference surface for stress computation is not straight-forward. The volume of each specimen can be estimated given its weight and the density of the printed material. An average surface can then be computed given the height of each specimen. This surface is used to estimate the compressive strength of each specimen given the maximum force it withstood. However, specimens L showed visible defects, one example being illustrated on Fig. 3 where there is no contact between the layers on the inside of the cylinder for approximately 1 cm, thus reducing the apparent cross-section. To account for the presence of those defects, the reference surface for specimens L is computed directly from the specimen dimensions as:

$$S = \pi \left(R_o^2 - \left(R_i + \ell_d \right)^2 \right) \tag{1}$$

where R_o and R_i are the outside and inside radii of the cylinder respectively, and $\ell_d = 10\,\mathrm{mm}$ is the estimated size of the defect.

2.2. Compressive strength results

The compressive strength results are gathered on Fig. 4. An example of hollow sample after failure is shown on Fig. 5. The compressive strength of printed samples increases from $72.3 \pm 1.7\,\mathrm{MPa}$ for the 24 mm thick samples (S) to $96.0 \pm 8.7\,\mathrm{MPa}$ for the 48 mm thick samples (L) stored in ambient conditions. Indeed, the thinner the wall, the lower the compressive strength.

The compressive strength of the samples which were kept in water reached $118.4 \pm 1.0\,\mathrm{MPa}$. This is close to the compressive strength of cast samples cured in water, which reached $113.9 \pm 0.9\,\mathrm{MPa}$ at 28 days. We thus postulate that the decrease of compressive strength is not due to a geometrical mechanical effect associated with layered structure but, rather, an effect due to a different evolution of the material during curing under given environmental conditions. Indeed, when suppressing evaporation in C samples, despite the layered hollow cylinder geometry, we retrieve strength levels similar to cast samples of the same initial material mix.

3. Model formulation

Printed parts have a high surface area exposed to evaporation, as opposed to cast parts, for which the formwork prevents evaporation when it is still present. As a result, the amount of water available for cement hydration is expected to be limited for printed parts, causing reduced material properties at the hardened state. Additionally, shrinkage is expected to be far more significant for printed parts since evaporation

Fig. 2. Printed specimens for compressive strength measurements.

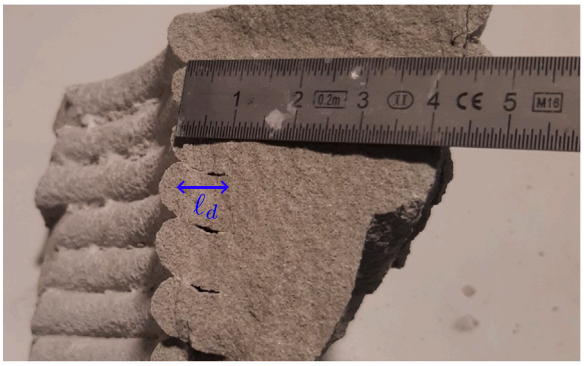

Fig. 3. Visible defect on a printed specimen of size L. On the inside of the cylinder, the layers are not contiguous.

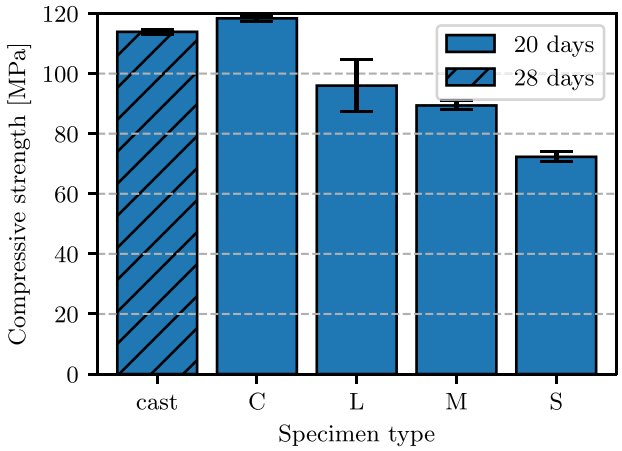

Fig. 4. Compressive strength results of printed and cast samples. The error bars represent the standard deviation.

could cause important suction in the pores, leading to plastic shrinkage before the strength build-up.

By considering the printing mix as a porous material, we propose a thermo-poro-mechanical model accounting for both water evaporation and cement hydration to represent the competition between hydration and drying. This model is an extension of a similar model developed in [32] which focused on early-age 3D-printed concrete evolution. The main mechanisms at play in the proposed model are illustrated on Fig. 6.

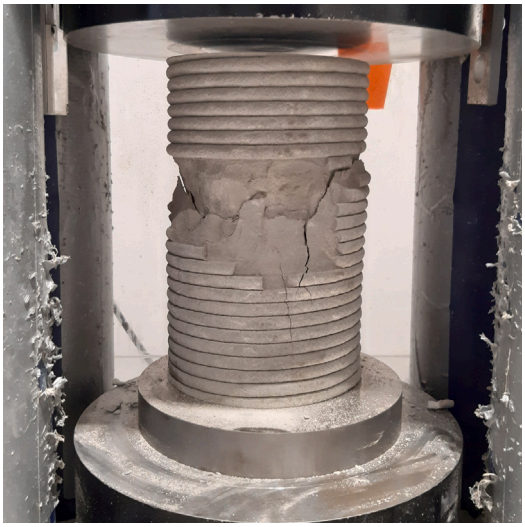

Fig. 5. Hollow cylinder after compressive strength measurement with a visible concrete cone failure.

3.1. Hydraulic modelling

Once added to the mix, water is progressively consumed by the hydration reaction to form cement hydrates. Additionally, water may evaporate from free surfaces in the absence of protective measures, as shown on Fig. 6. Here, the laws which describe water transport in the material, evaporation, and the total water conservation are presented.

3.1.1. Water transport and conservation

The printed material being porous, free water can be transported inside the material due to pressure gradients. The liquid water flux $\boldsymbol{w}$ is written as a function of the permeability k_ℓ of the porous material according to Darcy's law [33]:

$$\boldsymbol{w} = -\rho_w \frac{k_\ell}{\eta_w} \boldsymbol{\nabla} p \tag{2}$$

where $\rho_w = 1000\,\mathrm{kg\,m^{-3}}$ and $\eta_w = 1 \times 10^{-3}\,\mathrm{Pa\,s}$ are the water density and dynamic viscosity respectively, and p is the pore pressure. The permeability k_ℓ is assumed to depend on the porosity ϕ of the material and on the liquid saturation S_ℓ, that is the volume fraction of pores that is filled with water. The model proposed by Mualem [34] is used to represent the influence of the saturation on the permeability:

$$\frac{k_\ell(S_\ell)}{k_\ell(S_\ell = 1)} = \sqrt{S_\ell}\left(1 - \left(1 - S_\ell^{\frac{n}{n-1}}\right)^{\frac{n-1}{n}}\right)^2 \tag{3}$$

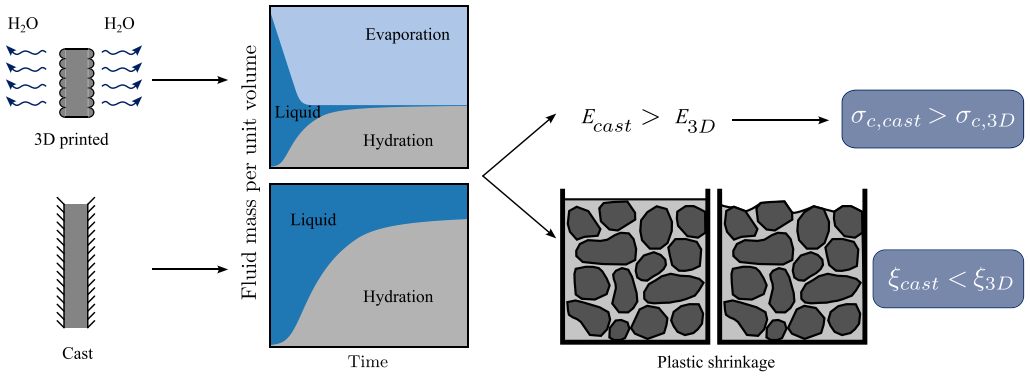

Fig. 6. Schematics of the mechanisms at play in the proposed model [31].

where n is a real exponent, here estimated at $n = 2.6$. Additionally, Taylor's model [35] is used to account for the variations of permeability with porosity, using the void ratio $e = \phi/(1-\phi)$:

$$\mathrm{d}\log_{10} k_\ell = \frac{\mathrm{d}e}{C_{k_\ell}} \tag{4}$$

where k_ℓ is in m^2 and C_{k_ℓ} is a constant, taken here as $C_{k_\ell} = 3.0$ [36]. The initial permeability is taken as $k_\ell = 1 \times 10^{-16}\,\mathrm{m}^2$. For the sake of simplicity, any initial heterogeneity in the material is neglected, in particular at the interface between two layers, although those interfaces have been shown in certain cases to provide heterogeneous transport properties due to a different microstructure and increased porosity [37].

Eventually, the total conservation of water can be written. At a given material point, the variations of water mass can be due to a transport phenomenon through the flux $\boldsymbol{w}$, or to the water consumption to form cement hydrates. In the present case of two-component (2K) 3D-concrete printing, two chemical reactions are taken into account. The extent of the activator reaction to form ettringites, which starts immediately after the activator is added to the printing mix, and the hydration extent of the actual setting of the cement paste, which starts several hours after printing, are denoted ξ_1 and ξ_2 respectively. The total conservation of water thus writes:

$$\frac{\mathrm{d}m_w}{\mathrm{d}t} = -\mathrm{div}(\boldsymbol{w}) - \sum_{i=1}^{2} \nu_{w,i} \mathcal{M}_w \frac{\mathrm{d}\xi_i}{\mathrm{d}t} \tag{5}$$

where $m_w = \rho_w S_\ell \phi$ is the water mass per unit volume, $\mathcal{M}_w = 18\,\mathrm{g\,mol}^{-1}$ is the molar mass of water and $\nu_{w,1} = 36$ [32] and $\nu_{w,2} = 18.5$ [28] are the stoichiometric coefficient of water consumption associated with each hydration reaction.

3.1.2. Evaporation modelling

The drying mechanism of porous media such as cement is described to happen in two phases [38,39]. The change of evaporation regime from a constant flux (in constant temperature conditions) to a decreasing flux corresponds to a change from a continuous liquid phase to a discontinuous liquid phase and a continuous gas phase in the porous system. Bakhshi et al. [38] estimate that the threshold at which this change happens can be linked to the degree of liquid saturation S_ℓ. For the sake of simplicity, here it is assumed it is rather linked to the mass of liquid water per unit volume $m_w = \rho_w S_\ell \phi$, as the variations of porosity ϕ are very small.

It is assumed here that the amount of water evaporated during the second evaporation phase, or capillary regime, is negligible compared to the amount evaporated during the constant drying rate regime. As a result, the falling drying rate stage is modelled with a null flux. For numerical reasons, the transition between the constant flux and null flux is done progressively between $m_w = 25\,\mathrm{kg\,m}^{-3}$ and $m_w = 75\,\mathrm{kg\,m}^{-3}$.

As to the first stage, the evaporation flux J is written as a function of the temperature T and relative humidity R_h as follows [40,41]:

$$J = A\left(R_{h,c} p_{sat}(T_c) - R_{h,a} p_{sat}(T_a)\right) \tag{6}$$

where index a and c refer to the air and cement respectively, p_{sat} is the saturated vapour pressure and A is a constant which can be determined experimentally. During this first phase, the relative humidity in the pores remains very close to 100%. Assuming the ambient conditions T_a and $R_{h,a}$ are constant, the computed flux only depends on the cement surface temperature, and is indeed constant if the surface temperature is constant.

The relative humidity $R_{h,c}$ of the porous material can be expressed as a function of the capillary pressure p_c and the temperature T according to Kelvin equation:

$$R_h = \exp\left(-\frac{p_c \mathcal{M}_w}{RT\rho_w}\right) \tag{7}$$

where $R = 8.314\,\mathrm{J\,K}^{-1}\,\mathrm{mol}^{-1}$ is the ideal gas constant. Assuming that the air pressure is equal to zero, the capillary pressure p_c is the opposite of the pore pressure p.

Eventually, the saturated vapour pressure can be directly estimated from the temperature according to norm EN ISO 13788 [42]:

$$p_{sat}(T) = 610.5 \exp\left(\frac{17.269T}{237.3+T}\right) \tag{8}$$

if $T \geq 0$ °C with T in °C and p_{sat} in Pa.

3.2. Thermal modelling

Heat transfers in the printed material are governed by conduction, and the temperature may raise due to the exothermic chemical reaction of cement hydration. Additionally, surface effects, including radiation, evaporative cooling and convection, can induce temperature variations.

3.2.1. Heat conduction and heat conservation

Heat transfers in the porous material are governed by Fourier's law, writing the heat flux $\boldsymbol{q}$ as a function of the temperature gradient:

$$\boldsymbol{q} = -k_T \boldsymbol{\nabla} T \tag{9}$$

where k_T is the thermal conductivity of the porous material, which is assumed to be constant equal to $k_T = 1.5\,\mathrm{W\,°C}^{-1}\,\mathrm{m}^{-1}$ [43]. Introducing this expression of the heat flux in the heat conservation equation, thermal equilibrium writes:

$$T\left(\frac{\partial S}{\partial t} - \mathrm{div}(s_w \boldsymbol{w})\right) = k_T \Delta T \tag{10}$$

where S is the total volume entropy of the material and s_w is the mass entropy of the fluid.

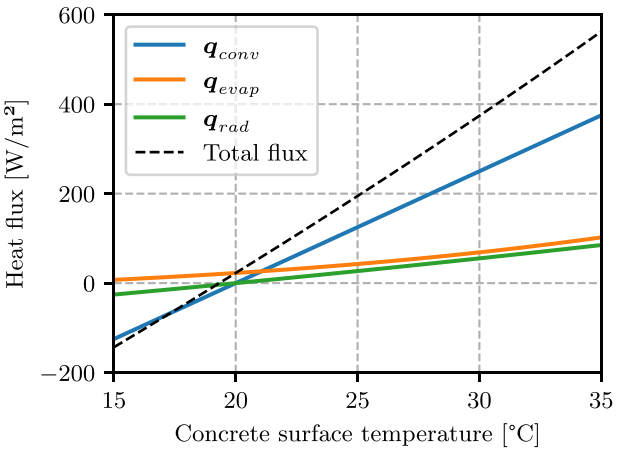

Fig. 7. Contribution of the convection q_{conv}, evaporation q_{evap} and radiation q_{rad} to the total heat flux for an air temperature $T_a = 20$ °C.

3.2.2. Temperature boundary condition

Heat transfers at the surface of the material are governed by several phenomena. First, the effect of air convection can be represented by a heat flux:

$$\boldsymbol{q}_{conv} = h\left(T_c - T_a\right)\boldsymbol{n} \tag{11}$$

where h is the heat transfer coefficient and $\boldsymbol{n}$ is the unit vector normal to the surface. In the present study, $h = 25$ W °C^{-1} m^{-2} is used, which provides an accurate representation of the material's temperature evolution. Evaporation also cools the material down. The associated heat flux is proportional to the water evaporation flux J and is written as:

$$\boldsymbol{q}_{evap} = \Delta H_{vap} J \boldsymbol{n} \tag{12}$$

where $\Delta H_{vap} = 2264\,\mathrm{kJ\,kg^{-1}}$ is the water enthalpy of vaporisation. Eventually, the printed piece can be heated or cooled due to the radiated energy, which is written according to Stefan–Boltzmann law:

$$\boldsymbol{q}_{rad} = \sigma\epsilon(T_c^4 - T_a^4)\boldsymbol{n} \tag{13}$$

where $\sigma = 5.67 \times 10^{-8}$ W °C^{-4} m^{-2} is Stefan–Boltzmann's constant and $\epsilon = 0.92$ is the emissivity of the material.

The contribution of evaporation, radiation and convection to the heat flux are illustrated on Fig. 7, showing that convection is the main factor contributing to the material cooling. However, it should be noted that the present study focuses on in-house printing. In the case of outdoor printing the influence of environmental factors would be different. In particular, direct sun radiation and wind could noticeably affect heat transfers and evaporation. Additionally, it can be noted that due to evaporation, the heat flux is not null when the air and concrete temperature are equal, but rather for a temperature such that the concrete surface is cooler than the air.

3.3. Thermo-poro-mechanical modelling

The printed concrete is modelled as a linear thermo-poro-elastic material. Denoting K its bulk modulus and K_s the bulk modulus of the solid skeleton, the Biot coefficient is computed as $b = 1 - K/K_s$. In this framework, three constitutive laws can be used to express the variations of stress $\mathrm{d}\boldsymbol{\sigma}$, porosity $\mathrm{d}\phi$ and solid entropy $\mathrm{d}S_s$ at a material point as a function of the strain $\boldsymbol{\epsilon}$, the temperature variations $T - T_0$ and the pore pressure variations $p - p_0$, T_0 and p_0 being the initial temperature and pore pressure respectively [44].

In a case where there is no cement hydration reaction, the material properties are constant and the air pressure is neglected, the stress tensor variations can be expressed as a function of the stiffness matrix $\mathbb{C}$:

$$\mathrm{d}\boldsymbol{\sigma} = \mathbb{C} : \mathrm{d}\boldsymbol{\varepsilon} - bS_\ell \mathrm{d}p\mathbf{1} - 3\alpha K \mathrm{d}T\mathbf{1} \tag{14}$$

where α is the thermal expansion coefficient of the material and $\mathbf{1}$ is the second order identity tensor. In the present study, values $K_s = 2{\times}10^{10}$ Pa and $\alpha = 1 \times 10^{-5}$ °C^{-1} are used. Similarly, porosity variations can be expressed as follows:

$$\mathrm{d}\phi = b\mathrm{tr}(\mathrm{d}\boldsymbol{\varepsilon}) + \frac{b - \phi_0}{K_s} S_\ell \mathrm{d}p - 3\alpha\left(b - \phi_0\right)\mathrm{d}T \tag{15}$$

where $\phi_0 = 0.25$ is the initial porosity [32], which corresponds here to the initial volume fraction of water. Eventually, the variation of solid entropy can be expressed as:

$$\mathrm{d}S_s = 3\alpha K \mathrm{tr}(\mathrm{d}\boldsymbol{\varepsilon}) - 3\alpha\left(b - \phi_0\right) S_\ell \mathrm{d}p + \frac{C\left(1 - \phi_0\right)}{T_0}\mathrm{d}T \tag{16}$$

where $C = 2.5 \times 10^6$ J °C^{-1} m^{-3} is the solid heat capacity at constant stress.

Eqs. (14) to (16) can be re-written to account for the variations of the material properties due to cement hydration. Pierre et al. [32] showed that two terms must be added to the set of equations to account for the increase of entropy and the variations of solid volume due to the chemical reaction. Assuming a linear superposition of the contributions of both hydration reactions, the material behaviour can be written as:

$$\begin{cases} \mathrm{d}\boldsymbol{\sigma} = \mathbb{C}(\xi) : \mathrm{d}\boldsymbol{\varepsilon} - b(\xi) S_\ell \mathrm{d}p\mathbf{1} - 3\alpha K(\xi)\mathrm{d}T\mathbf{1} \\ \mathrm{d}\phi = b(\xi)\mathrm{tr}(\mathrm{d}\boldsymbol{\varepsilon}) + \dfrac{b(\xi) - \phi_0(\xi)}{K_s} S_\ell \mathrm{d}p \\ \quad -3\alpha\left(b(\xi) - \phi_0(\xi)\right)\mathrm{d}T - \sum_{i=1}^{2} \Delta\overline{V}_{s,i}\mathrm{d}\xi_i \\ \mathrm{d}S_s = 3\alpha K(\xi)\mathrm{tr}(\mathrm{d}\boldsymbol{\varepsilon}) - 3\alpha\left(b(\xi) - \phi_0(\xi)\right) S_\ell \mathrm{d}p \\ \quad + \dfrac{C\left(1 - \phi_0(\xi)\right)}{T_0}\mathrm{d}T - \sum_{i=1}^{2} \dfrac{\mathcal{L}_i}{T_0}\mathrm{d}\xi_i \end{cases} \tag{17}$$

where $\xi = (\xi_1, \xi_2)$, and $\Delta\overline{V}_{s,i}$ and $\mathcal{L}_i$ represent the variations of molar volume of solid components and the latent heat associated with the hydration reaction i respectively. The values $\Delta\overline{V}_{s,1} = 5.85 \times 10^{-4}$ m^3 mol^{-1}, $\mathcal{L}_1 = 4.52 \times 10^5$ J mol^{-1} [45], $\Delta\overline{V}_{s,2} = 2.76 \times 10^{-4}$ m^3 mol^{-1} and $\mathcal{L}_2 = 2.0 \times 10^5$ J mol^{-1} [28] are used in the present study.

The porosity $\phi_0(\xi)$ represents the porosity of the material in the absence of thermo-poro-mechanical loading. It decreases when the hydration reactions progress due to the formation of cement hydrates that increase the total volume of solid as:

$$\mathrm{d}\phi_0(\xi) = -\sum_{i=1}^{2} \Delta\overline{V}_{s,i}\mathrm{d}\xi_i \tag{18}$$

3.4. Hydration model

An affinity-based model is used to describe the hydration kinetics. As proposed by Ulm et al. [26], the hydration kinetics is assumed to be proportional to the chemical affinity and to depend on the temperature according to an Arrhenius-type law:

$$\frac{\mathrm{d}\xi_i}{\mathrm{d}t} = \frac{\mathcal{A}_i}{\eta_{\xi_i}} \exp\left(-\frac{E_A}{RT}\right) \tag{19}$$

where $E_A = 4.5 \times 10^4$ J mol^{-1} is the hydration activation energy, R is the ideal gas constant and η_{ξ_i} is a viscosity which represents the effect of water diffusion through a layer of already formed hydrates, and increases with the hydration extent as:

$$\eta_{\xi_i} = \eta_{\xi_i,0} \exp\left(\overline{\eta}_i \frac{\xi_i}{\xi_i^\infty}\right) \tag{20}$$

where $\overline{\eta}_i$ and $\eta_{\xi_i,0}$ are material constants and ξ_i^∞ is the maximum hydration extent of reaction i, such that ξ_i/ξ_i^∞ is the dimensionless degree of hydration. It should be noted that ξ_i^∞ is not the total cement content, it is the maximum hydration value that can be reached in the material. Indeed, only a part of the cement in the material will be hydrated. As a result, the value of ξ_i^∞ is much lower than the total amount of cement added to the material. The values $\xi_1^\infty = 1\,\mathrm{mol\,m^{-3}}$

and $\xi_2^\infty = 470\,\mathrm{mol\,m^{-3}}$ are used in the present study. Those values will be further discussed in Section 6.3

Assuming that the free energy is a cubic function of the hydration extent, the chemical affinity can be written as [32]:

$$\mathcal{A}_i(\xi_i, R_h) = \min\left(1, 3.7R_h^{25}\right) k_{\xi_i} \left(\frac{\mathcal{A}_{i,0}}{k_{\xi_i}\xi_i^\infty} + \xi_i\right)\left(\xi_i^\infty - \xi_i\right) \tag{21}$$

Combining Eqs. (19) to (21), the hydration extent increment $\mathrm{d}\xi_i$ can be expressed as a function of 3 material parameters $k_{\xi_i}/\eta_{\xi_i,0}$, $\mathcal{A}_{i,0}/(k_{\xi_i}\xi_i^\infty)$ and $\overline{\eta}_i$ which can be determined experimentally by fitting experimental data from calorimetric measurements or P-wave modulus estimations:

$$\frac{\mathrm{d}\xi_i}{\mathrm{d}t} = \min\left(1, 3.7R_h^{25}\right) \frac{k_{\xi_i}}{\eta_{\xi_i,0}} \left(\frac{\mathcal{A}_{i,0}}{k_{\xi_i}\xi_i^\infty} + \xi_i\right)\left(\xi_i^\infty - \xi_i\right) \exp\left(-\overline{\eta}_i \frac{\xi_i}{\xi_i^\infty} - \frac{E_A}{RT}\right) \tag{22}$$

3.5. Complementary evolution laws

3.5.1. Retention curve

The liquid saturation is computed using the retention curve approach proposed by Van Genuchten [46], in which the liquid saturation is directly related to the capillary pressure p_c:

$$S_\ell = \left(1 + \left(\frac{p_c}{p_r}\right)^n\right)^{\frac{1-n}{n}} \tag{23}$$

where n is the same exponent as in Eq. (3) and p_r is a reference pressure which may vary as the cement hydration progresses, representing the variations of the microstructure. Here, an evolution of p_r proposed in [47] is used:

$$p_r(\xi_1, \xi_2) = p_{r,0} \exp\left(k_{sl,1}\frac{\xi_1}{\xi_1^\infty} + k_{sl,2}\frac{\xi_2}{\xi_2^\infty}\right) \tag{24}$$

taking $k_{sl,1} = 0$ and $k_{sl,2} = 1.64$, and using $p_{r,0} = 6.8 \times 10^5$ Pa.

3.5.2. Evolution of the stiffness with cement hydration

For simplicity, the printed material is modelled as a linear elastic isotropic material. As a result, the stiffness tensor $\mathbb{C}$ can be described by the Young modulus E and the Poisson ratio ν. Assuming that each hydration reaction has a linear contribution to the stiffness, the Young modulus is written as:

$$E = E_{\xi_1}\Delta\overline{V}_{s,1}\xi_1 + E_{\xi_2}\Delta\overline{V}_{s,2}\xi_2 \tag{25}$$

where E_{ξ_1} and E_{ξ_2} represent the stiffening due to the hydration increase. Assuming that the Poisson ratio of the solid skeleton is constant equal to 0.2 [48], the bulk modulus K and Biot coefficient b can then be computed given the Young modulus and the Poisson ratio.

3.5.3. Estimation of the compressive strength

The compressive strength of a wall section is estimated from the local stiffness values. Building codes usually provide an empirical relationship between the compressive strength σ_c and the Young modulus E of concrete as:

$$E = \beta\sigma_c^\gamma \tag{26}$$

where β and $\gamma < 1$ are constants. Eurocode 2 [49] uses $\beta = 22\,000/10^{0.3}$ and $\gamma = 0.3$ for E and σ_c in MPa, while ACI [50] uses $\beta = 4700$ and $\gamma = 0.5$ for traditional concrete. In the present study, the values of β and γ will be fitted to experimental data.

Table 1
Summary of the model parameters. The fit on ξ_2^∞ is done on compressive strength values at $R_h = 50\%$.

Parameter	Value	Determination
Fluid and heat transport		
Taylor permeability coefficient	$C_{k_\ell} = 3\,[-]$	[36]
Initial permeability	$k_0 = 1 \times 10^{-16}\,\mathrm{m^2}$	[32]
Heat transfer coefficient	$h = 25\ \mathrm{W\ °C^{-1}\ m^{-2}}$	Hypothesis
Thermal conductivity	$k_T = 1.5\ \mathrm{W\ °C^{-1}\ m^{-1}}$	[43]
Hydration kinetics		
Stoichiometric coefficient	$\nu_1 = 36\,[-]$	[32]
of water consumption	$\nu_2 = 18.5\,[-]$	[28]
Solid molar variations	$\Delta\overline{V}_{s,1} = 5.85 \times 10^{-4}\,\mathrm{m^3\,mol^{-1}}$	[47]
	$\Delta\overline{V}_{s,2} = 2.76 \times 10^{-4}\,\mathrm{m^3\,mol^{-1}}$	[28]
Latent heat of hydration	$\mathcal{L}_1 = 4.52 \times 10^5\,\mathrm{J\,mol^{-1}}$	[47]
	$\mathcal{L}_2 = 2.0 \times 10^5\,\mathrm{J\,mol^{-1}}$	[28]
Hydration activation energy	$E_A = 4.5 \times 10^4\,\mathrm{J\,mol^{-1}}$	[32]
Maximum hydration extent	$\xi_1^\infty = 1\,\mathrm{mol\,m^{-3}}$	[32]
	$\xi_2^\infty = 470\,\mathrm{mol\,m^{-3}}$	Fit
Thermo-poro-elastic parameters		
Solid skeleton bulk modulus	$K_s = 2 \times 10^{10}\,\mathrm{Pa}$	[32]
Solid thermal expansion coefficient	$\alpha = 1 \times 10^{-5}\,\mathrm{°C^{-1}}$	[51]
Initial porosity	$\phi_0 = 0.25\,[-]$	[32]
Solid capacity at constant stress	$C = 2.5 \times 10^6\ \mathrm{J\ °C^{-1}\ m^{-3}}$	[32]

Table 2
Measurements required to calibrate the model.

Parameters	Measurement method
Retention curve	Porosimetry
Hydration kinetics	Calorimetry or P-wave modulus
Stiffening coefficients	Young modulus short- and long-term
Compressive strength	Compressive strength short- and long-term
Evaporation rate	Mass loss measurements

Table 3
Estimated values of the parameters describing the retention curve.

Parameter	Value
Exponent of Van Genuchten model	$n = 2.6\,[-]$
Van Genuchten reference pressure	$p_{r,0} = 6.8 \times 10^5\,\mathrm{Pa}$
Coefficient of evolution	$k_{sl,1} = 0\,[-]$
of the retention curve	$k_{sl,2} = 1.64\,[-]$

4. Model calibration

The numerical values of the model parameters are given in Table 1. Most values are taken from the literature, and the sensitivity of the results on some parameters numerical values will be studied in Section 6.5.

Several parameters are left to be determined, which are specific to the printed material and may depend on the printing mix and process. They are listed in Table 2 along with a proposed measurement method.

4.1. Retention curve

The parameters of the retention curve were estimated by porosimetry, as described in [32]. The estimated values are given in Table 3.

4.2. Hydration kinetics and stiffening coefficients

The hydration kinetics are calibrated based on ultrasonic measurements of the P-wave modulus, assuming a linear relationship between the P-wave velocity and the hydration degree. The P-wave velocities were measured on a 2 cm thick sample, up to 24 h after printing as described in [32]. Given that the kinetics of each reaction can be described by three material parameters and two reactions are modelled,

Table 4
Estimated values of the parameters describing the hydration kinetics.

Parameter	Value
$k_{\xi_1}/\eta_{\xi_1,0}$	3.0×10^5 m^3 mol^{-1} s^{-1}
$\mathcal{A}_{1,0}/(k_{\xi_1}\xi_1^\infty)$	5.0×10^{-3} mol m^{-3}
$\overline{\eta}_1$	4 [–]
$k_{\xi_2}/\eta_{\xi_2,0}$	5.3 m^3 mol^{-1} s^{-1}
$\mathcal{A}_{2,0}/(k_{\xi_2}\xi_2^\infty)$	0.94 mol m^{-3}
$\overline{\eta}_2$	4 [–]

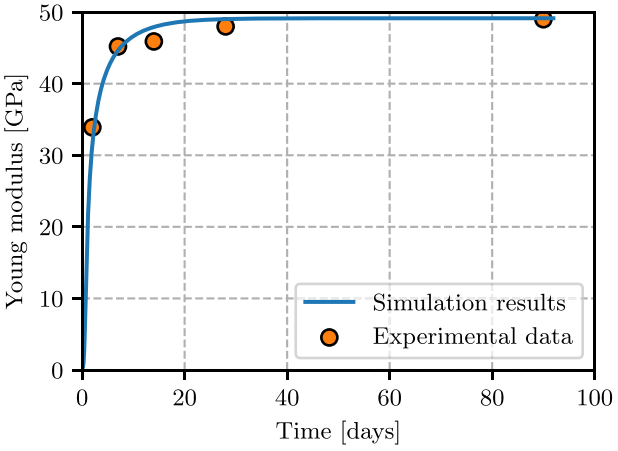

Fig. 8. Comparison of simulated hydration kinetics with experimental results.

six material parameters are estimated to best fit the experimental data. Their estimated values are given in Table 4.

The modelled evolution of the Young modulus is compared with experimental data, for which the Young modulus was measured according to norm ISO 1920-10 [52] on 11×22 cm cast cylinders cured in water from 2 to 90 days after mixing. A specimen in cured conditions (no evaporation, $T_a = 20$ °C) is simulated using the associated hydration kinetics, resulting in a homogeneous Young modulus. The coefficients in Eq. (25) are estimated to $E_{\xi_1} = 1.7 \times 10^4$ MPa and $E_{\xi_2} = 3.8 \times 10^5$ MPa. At longer time scales, the stiffness is mainly due to the cement hydration and $E \simeq E_{\xi_2} \Delta\overline{V}_{s,2}\xi_2^\infty$. The computed evolution of the Young modulus E is represented on Fig. 8, showing that the model estimation is in accordance with experimental data and thus further validating the hydration kinetics model.

4.3. Compressive strength

By fitting measurements of the Young modulus and compressive strength obtained after 2 to 90 days on cast cylinders cured in water, coefficients β and γ in Eq. (26) are estimated to $\beta = 19\,000/10^{0.38}$ and $\gamma = 0.38$:

$$E = 19\,000 \times \left(\frac{\sigma_c}{10}\right)^{0.38} \tag{27}$$

with E and σ_c in MPa. The correlation results are illustrated on Fig. 9 for the Eurocode 2, ACI and proposed estimations.

4.4. Evaporation rate

The evaporation rate was measured by monitoring the total mass of a $260 \times 40 \times 90$ mm sample cut from a fresh printed wall for 5 h after printing. The surface temperature of the sample was also monitored, as well as the ambient temperature and relative humidity of the room. The experimental setup is shown on Fig. 10. The ambient temperature in the room was observed to be very stable, varying from 19.8 °C to 20.8 °C. The relative humidity was also stable at 60% before printing,

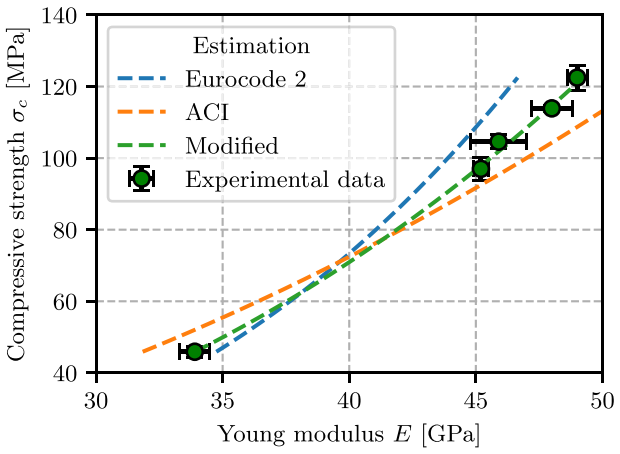

Fig. 9. Compressive strength σ_c as a function of the Young modulus E: comparison of the models with experimental data.

Fig. 10. Experimental setup to measure the evaporation rate and monitor the surface and air temperature.

and reached 70% 3 h after the end of the wall print due to the room and the printer being cleaned at that time.

The surface of the printed specimen being estimated at 645 cm^2, evaporation measurements provided a constant flux value $J = 1 \times 10^{-5}$ kg m^{-2} s^{-1} after 3 h, yielding $A = 1.07 \times 10^{-8}$ s m^{-1} assuming $T_c = T_a = 20$ °C, $R_{h,c} = 100\%$ and $R_{h,a} = 60\%$. The surface estimation is not straight-forward due to the presence of heterogeneities resulting from the layer-by-layer deposition. Here the surface is estimated by considering a smooth surface. This choice is discussed in Section 6.1.

The modelled and measured cumulative mass loss are represented on Fig. 11 for comparison. The modelled material is simulated using $T_c(t = 0) = 35$ °C, $T_a = 20$ °C and $R_{h,a} = 60\%$. The measured evaporation rate is initially not constant and decreases progressively until reaching a steady value 3 h after printing. These variations can be explained by the associated temperature decrease. Indeed, the specimen surface temperature is initially more than 10 °C warmer than the ambient air and decreases progressively until it reaches the air temperature. This initial temperature difference is attributed to self-heating due to viscous

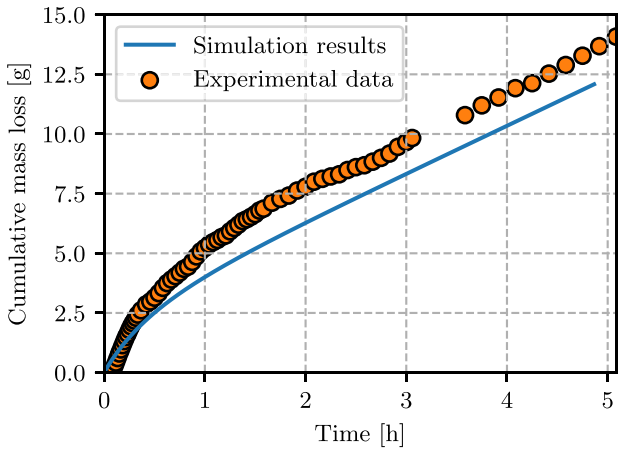

Fig. 11. Cumulative mass loss measured on a $260 \times 40 \times 90$ mm printed specimen.

dissipation in the extruder and the influence of the aluminium sulphate activator [53]. The modelled evaporation rate is initially lower than the measured rate. This is likely due to increased convection at the beginning of the measurements, caused by ongoing activity in the printing room.

5. Results and model validation

5.1. Simulation conditions

A printed wall in the (e_y, e_z) plane is considered here. Neglecting boundary effects, the geometry is invariant along directions e_y and e_z. The study is therefore reduced to a small wall section of arbitrary height W in the y direction, as illustrated on Fig. 12. Assuming the wall plane is a symmetry plane, the study is further reduced to a half-thickness sample. For the sake of simplicity, the wall surface heterogeneity due to the layer-by-layer deposition is not simulated, and a simple rectangular shape is used instead. The initial concrete temperature T_c, ambient air temperature T_a and relative humidity $R_{h,a}$ are imposed, and the associated evaporation flux and heat flux on the free boundary are computed.

The simulations are performed using FEniCSx Python interface [54], and the material model is implemented in MFront [55] to solve the problem with full coupling using the `dolfinx_materials` package[1] [56]. The mesh is composed of 50 2D plane strain rectangular elements which are refined at the boundary, as visible on Fig. 12. Although the mesh contains a relatively low number of elements, a comparison in Section 5.3 shows that the results are well converged. The displacement u is taken as a second order Lagrange element, and the temperature T and pressure p are taken as first order Lagrange elements.

5.2. Early-age temperature variations

The modelled and measured surface temperature evolution are illustrated on Fig. 13, showing that the model explains well the temperature decrease during drying. The slight temperature elevation measured between 4 and 5 h after printing is mainly attributed to the absence of control of the ambient air temperature.

The initial temperature difference between the air and the printed material significantly increases evaporation. Indeed, the measured initial evaporation flux J reaches $5 \times 10^{-5}\,\mathrm{kg\,m^{-2}\,s^{-1}}$, and progressively decreases as the material temperature decreases, until the flux reaches a constant value of $1{\times}10^{-5}\,\mathrm{kg\,m^{-2}\,s^{-1}}$. This highlights the strong influence of the material temperature on the amount of water available for cement hydration. As a result, measuring the material temperature as it is deposited, through a temperature sensor in the printing head for instance, can help better assess drying to better estimate the hardened properties of the material.

5.3. Compressive strength at the hardened state

The relative humidity was not monitored between the printing session and the compressive strength measurements. As a result, there are some uncertainties on its value. The compressive strength is therefore simulated after 20 days at 3 different relative humidities ranging from 40% to 60%, at a constant air temperature $T_a = 20$ °C and with an initial concrete temperature $T_c = 35$ °C. The results are illustrated on Fig. 14, showing good agreement with experimental data for $R_{h,a} = 50\%$, although the model seems to overestimate the influence of the wall thickness on the compressive strength. We must however recall the uncertainties associated with the defects observed with such larger specimens.

The obtained water mass per unit volume m_w and Young modulus profiles along the cross-section are illustrated on Fig. 15 up to 7 days after printing, showing that even if the water profiles are not homogeneous, a slight decrease being visible close to the evaporation surface, the obtained Young modulus profiles are homogeneous and no dry front effect is visible. The local compressive strength, which is estimated by Eq. (27), and the global compressive strength of the cross-section, which is the average of the local compressive strength over the cross-section, coincide in the present case.

The water mass per unit volume m_w and Young modulus profiles along the cross-section obtained for a refined mesh with 200 rectangle elements instead of 50 are illustrated on Fig. 16 up to 7 days after printing, showing that refining the mesh does not affect the obtained profiles, and that the results are well converged.

5.4. Plastic shrinkage

Crack opening resulting from shrinkage was measured 24 h after printing on 2 m long printed walls for two wall thicknesses 22 mm and 40 mm, in two different curing conditions. Exposed specimens were left in the ambient air with no protective measures to prevent evaporation, and protected specimens were put in a sealed container to create a humid curing environment. Displacement at the bottom of the walls was made possible by lubricating the contact surface with oil, and displacement on the ends of the walls was blocked by inserting vertical columns on both ends. The experimental setup is illustrated in 17.

Crack opening is not equivalent to shrinkage strains but rather provides a lower bound of the shrinkage strains. However, crack opening results can be compared to assess the influence of the drying environment and the wall thickness on plastic shrinkage.

After 24 h, no cracks were visible on the specimens which were kept in a sealed container. Simulation results do provide non-negligible strains, reaching $1.5\,\mathrm{mm\,m^{-1}}$ after 24 h, regardless of the wall thickness. In the absence of evaporation, this modelled shrinkage corresponds to the autogenous shrinkage of the material, and the obtained value is consistent with what can be found in the literature for high performance cement pastes [57].

The absence of cracks for the specimens in a sealed container shows that crack opening is not a direct measurement of shrinkage strains. Indeed, with the presented experimental setup, shrinkage may result in stress build-up in the structure which may not result in cracks if stresses are too low, and the sides of the structure itself may deform if not rigid enough, limiting the crack opening.

As to the exposed specimens, 22 mm and 40 mm thick walls resulted in 4.5 mm and 2.5 mm wide cracks respectively. Comparatively, simulation results respectively predict $3.8\,\mathrm{mm\,m^{-1}}$ and $2.7\,\mathrm{mm\,m^{-1}}$ strain levels

[1] Available at https://github.com/bleyerj/dolfinx_materials.

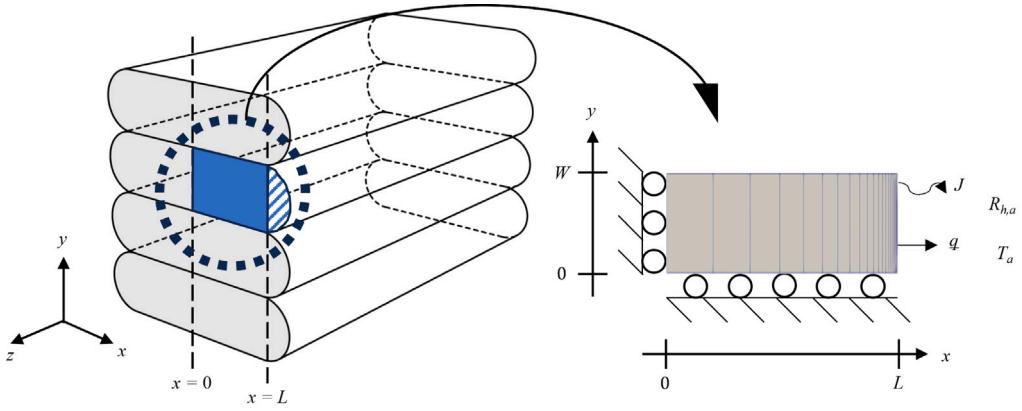

Fig. 12. Schematics of the simulated geometry and boundary conditions.

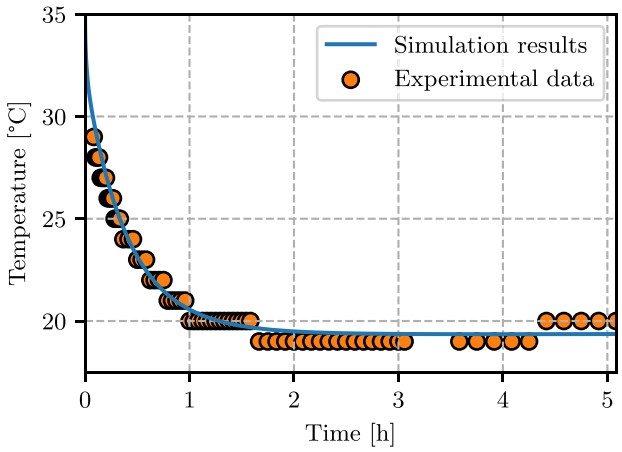

Fig. 13. Surface temperature evolution of the printed specimen: comparison of the simulation results with experimental data (1 °C accuracy of the thermal sensor).

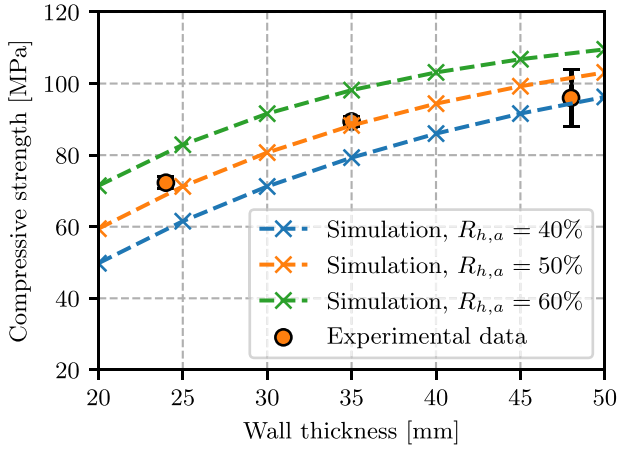

Fig. 14. Simulated and measured compressive strength as a function of the wall thickness 20 days after printing. The error bars represent the standard deviation.

for the two studied wall thicknesses. Such simulated strain results are consistent with what can be found in the literature [10,12,13]. Fig. 18 shows both evolutions of experimentally measured crack openings and simulated shrinkage strains as a function of the wall thickness. We can observe a similar decrease of the measured crack openings and simulated shrinkage strains as a function of the wall thickness, showing that the model predicts a dependency of the shrinkage strain levels on the wall thickness consistent with the observed crack openings.

6. Discussion

6.1. Surface effect on the evaporation rate

The estimation of the surface does not take into account the layer geometry but rather the smooth surface. Indeed, a comparison shown on Fig. 19 of evaporation results for a smoothed specimen (Fig. 20, top), for which heterogeneities were cut immediately after the end of printing, and a specimen with heterogeneities due to the layer by layer deposition (Fig. 20, bottom) showed that the presence of the heterogeneities does not affect evaporation, indicating that taking the smooth surface as a reference is correct.

6.2. Influence of the wall thickness

6.2.1. On the compressive strength

As illustrated on Fig. 14, the model allows to explain the influence of the wall thickness on the compressive strength. This influence can be explained by simple dimensional reasoning, similar to [58] where the reasoning is presented for 3D-printed earth walls. On the one hand, the total mass of evaporated water at a given time $m_{evap} = \int_0^t J(t)\mathrm{d}t$ is proportional to the surface over which evaporation occurs, denoted S. On the other hand, the total mass of water consumed by the hydration reaction $m_{cons} = \sum_{i=1}^{2} \nu_i \mathcal{M}_w \xi_i$ is proportional to the volume V of the specimen. Therefore, the ratio V/S which corresponds to the wall thickness L represents the relative influence of hydration compared to evaporation. For thin specimens, evaporation becomes dominant and the amount of liquid water in the material quickly diminishes, thus limiting cement hydration and structural build-up. For thick specimens, evaporation becomes negligible and hydration and structural build-up can occur without impediment.

Figs. 21(a) and 21(b) represent the simulated evolution of the water mass distribution in thin (20 mm) and thick (50 mm) specimens respectively. During the first evaporation phase (1 to 2 days here), the evaporation flux is constant and the total mass of water in the material decreases linearly with a slope $-J/L$. When the wall is thinner and L decreases, the slope increases and the amount of water available for cement hydration rapidly diminishes, thus reducing the possible stiffness and compressive strength build-up.

6.2.2. On the plastic shrinkage

In the absence of protective measures to prevent evaporation, the plastic shrinkage decreases when the wall thickness increases. Since the surface evaporation rate does not depend on the wall thickness [12] in the first phase of drying, the total volume of evaporated water

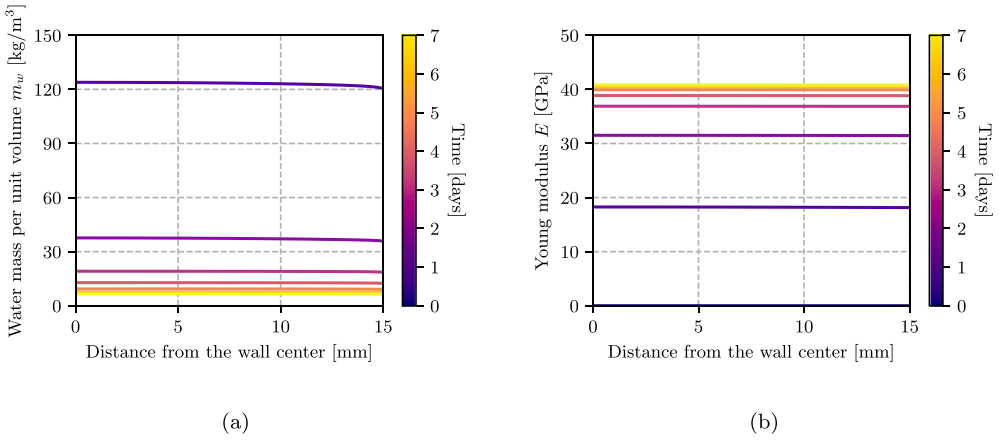

Fig. 15. Simulated water mass per unit volume m_w (a) and Young modulus E (b) at different times after printing, for an ambient air at $R_h = 50\%$.

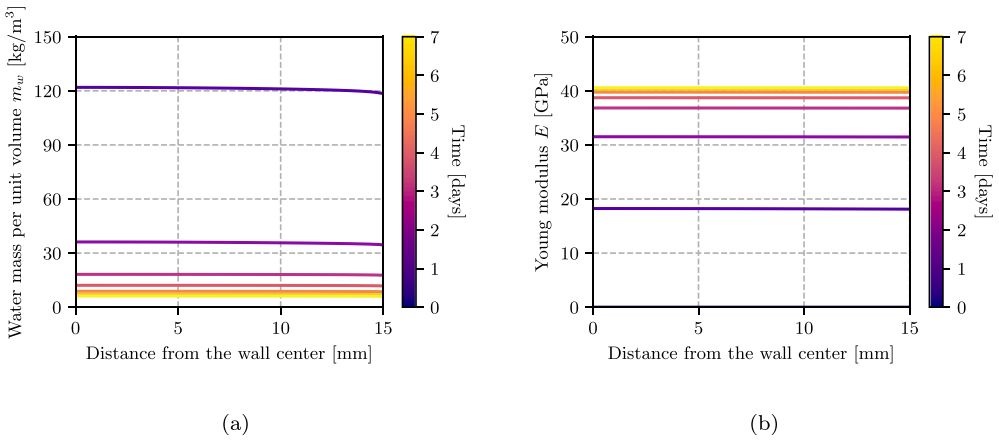

Fig. 16. Simulated water mass per unit volume m_w (a) and Young modulus E (b) at different times after printing, for an ambient air at $R_h = 50\%$ for a refined mesh with 200 rectangle elements.

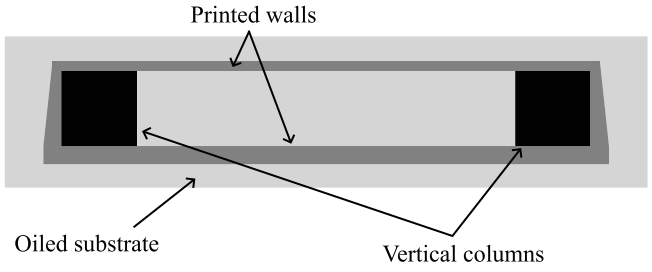

Fig. 17. Experimental setup (top view) used for measuring crack opening.

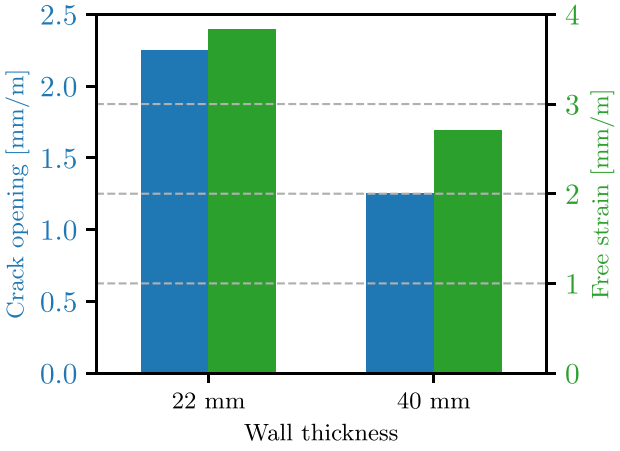

Fig. 18. Crack opening measured on printed walls and simulated free strain obtained for air-exposed specimens 24 h after printing.

after a given time is identical for both wall thicknesses, resulting in a volume rate of evaporation which is inversely proportional to the wall thickness, and thus greater shrinkage for thinner walls. This phenomenon has been discussed in [12].

In the case of cured specimens for which evaporation is not possible, the wall thickness has little to no influence on plastic shrinkage. At very early age, the modelled specimens are warmer than the air and the evaporation flux is not null, although it is low, resulting in a slight influence of the wall thickness on the plastic shrinkage results.

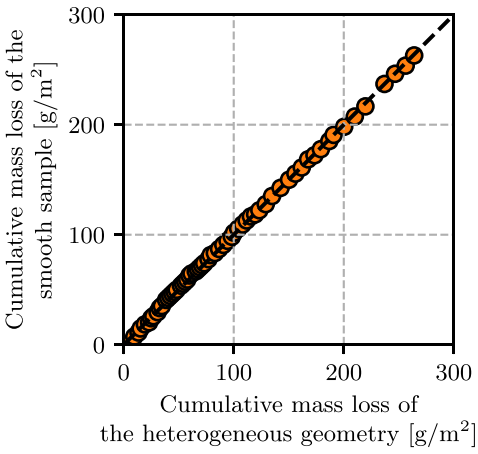

Fig. 19. Cumulative mass loss measured on a smooth specimen as a function of the cumulative mass loss measured on a heterogeneous specimen.

Fig. 20. Smooth sample (top) and heterogeneous sample (bottom) used for evaporation measurements.

Fig. 22 illustrates the shrinkage results for three wall thicknesses and two ambient conditions. For a given relative humidity, shrinkage strain increases as the wall thickness decreases. As expected, the influence of the wall thickness on plastic shrinkage is reduced when the relative humidity increases.

6.3. Value of the maximum hydration extent

The value of the maximum hydration extent, which corresponds to the maximum amount of cement that can be hydrated, is unknown. The value $\xi_2^\infty = 470\,\mathrm{mol\,m^{-3}}$ used in this work was estimated to obtain the best fit (in the sense of the least square method) between the compressive strength results simulated at 50% relative humidity and experimental data. The fit is illustrated on Fig. 23 for 3 values of the maximum hydration extent ξ_2^∞. It should be noted that changing the value of the maximum hydration extent ξ_2^∞ requires to change the values of the hydration kinetics and stiffness build-up parameters, so that their evolution in time remain unchanged in saturated conditions, which were the calibration conditions.

Increasing the stiffness value by a given amount requires more water consumption when the value of the maximum hydration extent is increased. As a result, for a given quantity of available water for cement hydration, the reachable stiffness and compressive strength values diminish when the maximum hydration extent in the model increases. This phenomenon is observed on Fig. 23 where the highest compressive strength values are obtained for the lowest maximum hydration extent.

6.4. Influence of the curing conditions

It was shown that printed structures loose a significant amount of water within a short time after printing due to their high exposed surface and the absence of formwork, thinner structures being more exposed to both plastic shrinkage and a limited stiffness and compressive strength build-up. Those two observations outline the importance of controlling the curing environment of printed parts.

Significant plastic shrinkage occurs due to evaporation a couple hours after printing. For large printed parts, this shrinkage can even be visible before the end of printing. Since it is difficult to prevent evaporation during the printing phase, plastic shrinkage effects could rather be limited by adapting the design of the printed parts to account for the deformations to come, similar to what was proposed by [59] to account for deformations during printing.

As to the compressive strength and stiffness build-up, it is important to ensure that there is enough water available in the material to allow for sufficient cement hydration. Once the fabricated part is fully printed and has reached a minimum stiffness, it is easier to control the relative humidity at which it is stored, by wetting it with water, protecting it by a cover or putting it in a humid environment or a sealed container for instance.

The presented model can be used to simulate varying ambient conditions to estimate their efficiency to reach a target compressive strength. However, it should be noted that no experiments were done to study the validity of the evaporation model in the case of a dry material capturing water from its environment.

6.5. Sensitivity study

The model contains many input parameters, some of which may vary from one printing session to another, or have highly uncertain values.

6.5.1. Influence of the material's initial temperature

The material temperature at the nozzle is a model input, which may vary depending on the material viscosity, pipe length and amount of activator added to the mix. Since its value has a direct influence on the evaporation flux, it may have a significant influence on the simulation results. The influence of the material's initial temperature on shrinkage 5 h after printing is shown on Fig. 24 for several wall thicknesses, simulating an ambient air for which $R_h = 50\%$ and $T_a = 20\ ^\circ\mathrm{C}$. As expected, higher initial temperatures lead to higher evaporation, resulting in more significant shrinkage. Additionally, it is observed that the simulated shrinkage is linearly correlated to the initial material temperature.

6.5.2. Influence of the retention curve parameters

The reference pressure $p_{r,0}$ and coefficient $k_{sl,2}$ describing the retention curve may greatly vary from one material to another, and some uncertainty on their values remain. Shrinkage resulting from simulations with various values of the reference pressure $p_{r,0}$ is represented on Fig. 25, showing a positive correlation between plastic shrinkage and the reference pressure. Plastic shrinkage measured on printed parts left without curing measures to prevent evaporation typically reaches $3\,\mathrm{mm\,m^{-1}}$ to $4\,\mathrm{mm\,m^{-1}}$ for thin walls [12,31], further validating the chosen value of the reference pressure $p_{r,0}$.

Shrinkage results 5 h after printing do not depend on the value of $k_{sl,2}$, since the hydration extent ξ_2/ξ_2^∞ is negligible at that time, and the water retention curve has not shifted yet.

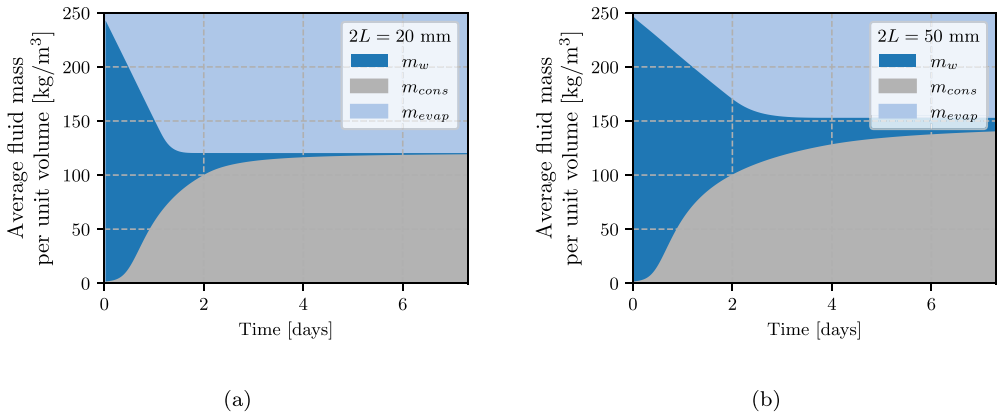

Fig. 21. Modelled evolution of the water mass distribution for 20 mm thick (a) and 50 mm thick (b) specimens at 50% relative humidity. m_{evap} and m_{cons} are respectively the evaporated water mass per unit volume and the water mass consumed by the hydration reaction per unit volume.

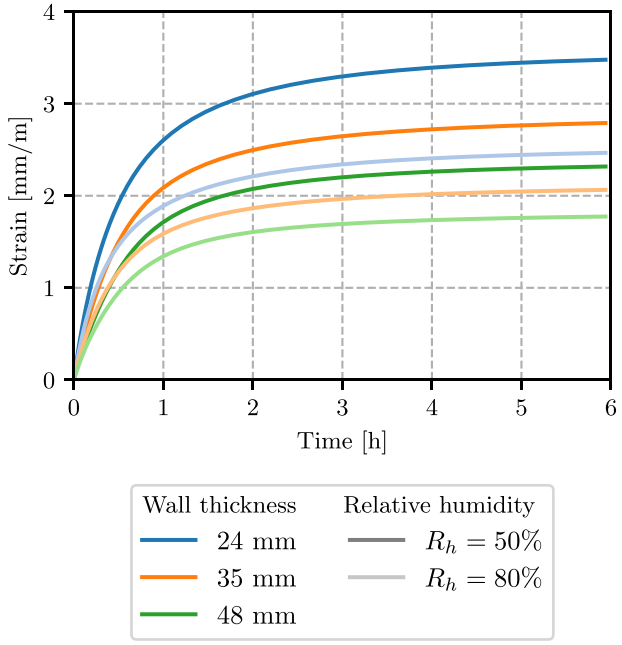

Fig. 22. Simulated evolution of the shrinkage for several wall thicknesses and ambient relative humidities.

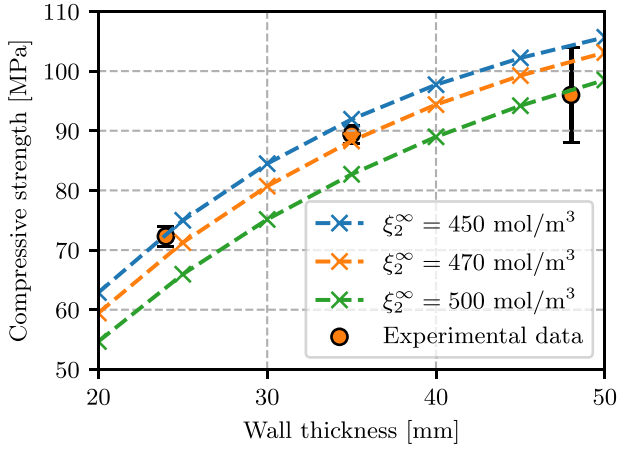

Fig. 23. Calibration of the maximum hydration extent ξ_2^∞ based on the compressive strength results.

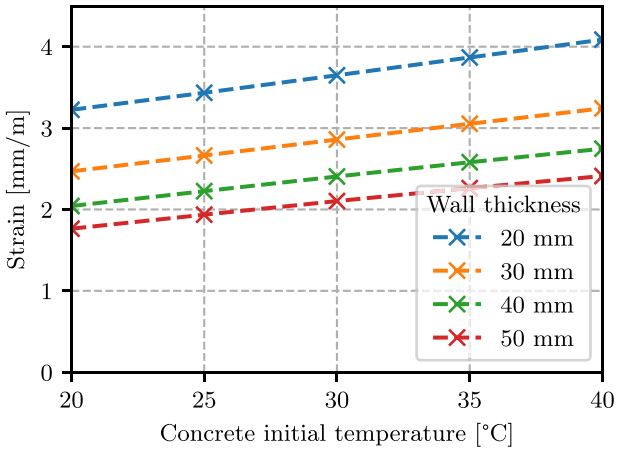

Fig. 24. Simulated influence of the initial material temperature on shrinkage 5 h after printing, for a modelled ambient air at $R_h = 50\%$ and $T_a = 20$ °C.

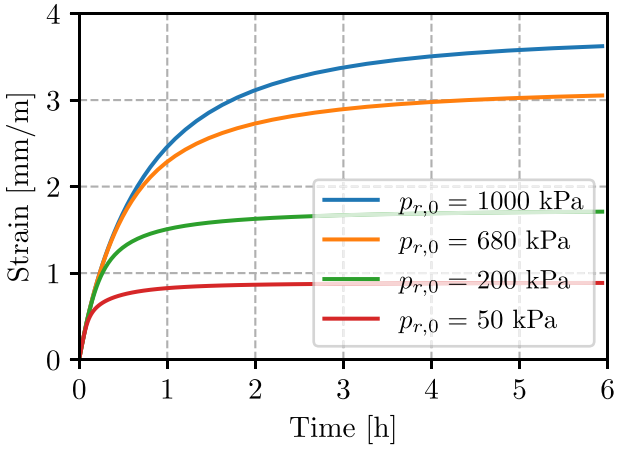

Fig. 25. Influence of the reference pressure $p_{r,0}$ on the modelled shrinkage for an ambient air at $R_h = 50\%$ and $T_a = 20$ °C and a 30 mm thick wall.

For $k_{sl,2}$ varying from 1 to 4, the modelled water content and hydration extent are homogeneous in the wall thickness at 7 days, and no gradient of those values can be observed. However, the Young modulus does depend on the value of $k_{sl,2}$, as shown on Fig. 26. The lower the value of $k_{sl,2}$, the higher the Young modulus at 7 days. Indeed, evaporation is unaffected by the value of $k_{sl,2}$. As a result, the

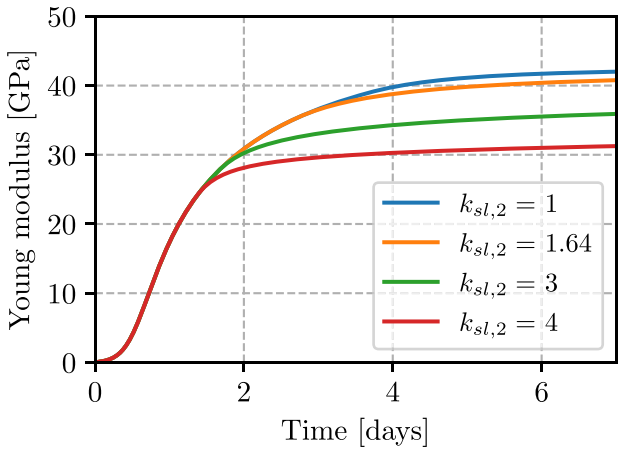

Fig. 26. Influence of the value of the coefficient of evolution of the retention curve $k_{sl,2}$ on the modelled Young modulus for an ambient air at $R_h = 50\%$ and $T_a = 20$ °C.

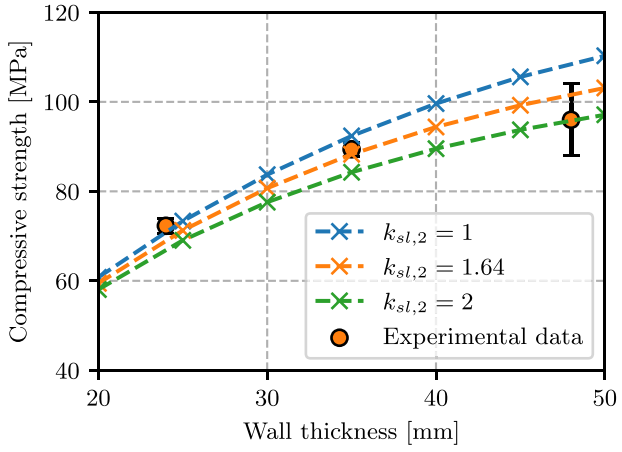

Fig. 27. Compressive strength at 20 days as a function of the wall thickness for an ambient air at $R_h = 50\%$ and $T_a = 20$ °C, for various values of the coefficient of evolution of the retention curve $k_{sl,2}$.

saturation S_ℓ at a given time does not depend on the value of $k_{sl,2}$. However, the capillary pressure increases as $k_{sl,2}$ increases for a given saturation level, and the pore relative humidity decreases, slowing down the hydration kinetics. Subsequently, the hydration extent and Young modulus are lower for higher values of $k_{sl,2}$. Results in terms of compressive strength at 20 days as a function of the wall thickness are illustrated on Fig. 27, showing that the simulation of the compressive strength is relatively sensible to the value of $k_{sl,2}$, as expected from its influence on the Young modulus evolution.

7. Conclusions

The present study confirms that extrusion-based 3D-printed concrete is subject to high water loss in the absence of curing measures to prevent evaporation due to the large surface to volume ratios of printed parts. This evaporation, which depends on the surface area exposed to the ambient air, has visible detrimental effects short-term on the plastic shrinkage and long-term on the stiffness and compressive strength. The main outcomes of the present study are as follows:

- In the absence of curing, the compressive strength of printed parts can decrease by more than 35% for 24 mm thick walls compared to cast specimens of the same material. Placing the printed parts in water to prevent any evaporation allows to reach the compressive strength of the cast specimens.
- 20 days after printing, the compressive strength of printed parts depends on the wall thickness. This phenomenon, which is well captured by the presented coupled model, is due to the variations of the surface-to-volume ratio, thinner walls resulting in higher evaporation, lower cement hydration and lower compressive strength. The modelled coupling between evaporation, cement hydration and strength build-up allows to capture this phenomenon and estimate the mechanical properties of a printed sample in given ambient conditions.
- The fully coupled model can also be used to estimate plastic shrinkage induced by water evaporation. Similarly, plastic shrinkage is more prominent for thinner walls due the higher surface-to-volume ratio. Effects of plastic shrinkage are visible just a couple hours after printing, when the stiffness build-up is limited.

Those results outline the importance of mastering the curing conditions at which printed parts are stored immediately after printing. Indeed, a humid environment, although restricting in terms of feasibility, provides better results in terms of compressive strength build-up and limited plastic shrinkage. Additionally, limiting air convection around fresh printed parts and reducing the temperature difference between the material and the ambient air allow to reduce evaporation, improving both shrinkage results and mechanical performances of the material.

Eventually, the proposed model can be used to simulate curing procedures, and estimate their short-term efficiency in terms of shrinkage, and long-term efficiency in terms of mechanical performance. Inversely, given process control data such as the material temperature at the nozzle and curing measures, the model can be used to compute the reachable mechanical properties. Additionally, although the model has numerous input parameters, most values are determined from distinct experimental procedures. Moreover, the sensitivity study presented in this work emphasises the robustness of the model to variations of the least well-known parameters, making the model useable in practice, even with process variability. An interesting perspective would be to rely on uncertainty quantification techniques to more precisely assess the influence of model parameter uncertainties on various quantities of interest.

The fine process control allowed by additive manufacturing during and after printing opens the door to using digital twins to adjust printing parameters in real time in order to obtain printed parts with the desired properties. Additionally, the possibility of having fine control of the printing environment and estimating the final properties of the material in a given environment could open the door to specific standardisation, with relevant safety coefficients.

CRediT authorship contribution statement

Alice Gribonval: Writing – review & editing, Writing – original draft, Visualization, Software, Methodology, Data curation, Conceptualization. **Maxime Pierre:** Software, Methodology, Conceptualization. **Nicolas Ducoulombier:** Writing – review & editing, Supervision, Methodology, Conceptualization. **Karam Sab:** Writing – review & editing, Supervision, Methodology, Conceptualization. **Romain Mesnil:** Writing – review & editing, Supervision, Methodology, Conceptualization. **Jérémy Bleyer:** Writing – review & editing, Supervision, Software, Methodology, Conceptualization.

Declaration of competing interest

The authors declare that they have no known competing financial interests or personal relationships that could have appeared to influence the work reported in this paper.

Acknowledgements

This material is based upon work supported by the ANRT (Association nationale de la recherche et de la technologie) with a CIFRE fellowship granted to Alice Gribonval (grant n° 2024/0310). The authors express their acknowledgements to XtreeE's team and to Marc Quiertant from Université Gustave Eiffel for his help on the compressive strength measurements.

Data availability

Data will be made available on request.

References

[1] G. De Schutter, K. Lesage, V. Mechtcherine, V.N. Nerella, G. Habert, I. Agusti-Juan, Vision of 3D printing with concrete — Technical, economic and environmental potentials, SI : Digital concrete 2018, Cem. Concr. Res. 112 (2018) 25–36, http://dx.doi.org/10.1016/j.cemconres.2018.06.001.

[2] C. Gosselin, R. Duballet, P. Roux, N. Gaudillière, J. Dirrenberger, P. Morel, Large-scale 3D printing of ultra-high performance concrete – a new processing route for architects and builders, Mater. Des. 100 (2016) 102–109, http://dx.doi.org/10.1016/j.matdes.2016.03.097.

[3] Z. Zhao, C. Ji, J. Xiao, L. Yao, C. Lin, T. Ding, T. Ye, A critical review on reducing the environmental impact of 3D printing concrete: Material preparation, construction process and structure level, Constr. Build. Mater. 409 (2023) 133887, http://dx.doi.org/10.1016/j.conbuildmat.2023.133887.

[4] S. Lim, R. Buswell, T. Le, S. Austin, A. Gibb, T. Thorpe, Developments in construction-scale additive manufacturing processes, Autom. Constr. 21 (2012) 262–268, http://dx.doi.org/10.1016/j.autcon.2011.06.010.

[5] I. Hager, A. Golonka, R. Putanowicz, 3D printing of buildings and building components as the future of sustainable construction? Procedia Eng. 151 (2016) 292–299, http://dx.doi.org/10.1016/j.proeng.2016.07.357, Ecology and new building materials and products 2016.

[6] S. El-Sayegh, L. Romdhane, S. Manjikian, A critical review of 3D printing in construction: benefits, challenges, and risks, Arch. Civ. Mech. Eng. 20 (2) (2020) 34, http://dx.doi.org/10.1007/s43452-020-00038-w.

[7] F.P. Bos, C. Menna, M. Pradena, E. Kreiger, W.R.L. da Silva, A.U. Rehman, D. Weger, R.J.M. Wolfs, Y. Zhang, L. Ferrara, V. Mechtcherine, The realities of additively manufactured concrete structures in practice, Cem. Concr. Res. 156 (2022) 106746, http://dx.doi.org/10.1016/j.cemconres.2022.106746.

[8] G. Ma, R. Buswell, W.R. Leal da Silva, L. Wang, J. Xu, S.Z. Jones, Technology readiness: A global snapshot of 3D concrete printing and the frontiers for development, Cem. Concr. Res. 156 (2022) 106774, http://dx.doi.org/10.1016/j.cemconres.2022.106774.

[9] L. Thomas-Seale, J. Kirkman-Brown, M. Attallah, D. Espino, D. Shepherd, The barriers to the progression of additive manufacture: Perspectives from UK industry, Int. J. Prod. Econ. 198 (2018) 104–118, http://dx.doi.org/10.1016/j.ijpe.2018.02.003.

[10] G.M. Moelich, J. Kruger, R. Combrinck, Plastic shrinkage cracking in 3D printed concrete, Compos. Part B: Eng. 200 (2020) 108313, http://dx.doi.org/10.1016/j.compositesb.2020.108313.

[11] G.S. Slavcheva, Drying and shrinkage of cement paste for 3D printable concrete, IOP Conf. Ser.: Mater. Sci. Eng. 481 (1) (2019) 012043, http://dx.doi.org/10.1088/1757-899X/481/1/012043.

[12] S. Markin, R. Combrinck, V. Mechtcherine, Specifics of plastic shrinkage in 3D-printed concrete elements, Cem. Concr. Res. 184 (2024) 107512, http://dx.doi.org/10.1016/j.cemconres.2024.107512.

[13] K. Xia, Y. Chen, Y. Chen, Z. Jia, L. Jia, Y. Gao, Y. Zhang, Understanding and modeling the plastic deformation of 3D printed concrete based on viscoelastic creep behavior, Addit. Manuf. 84 (2024) 104132, http://dx.doi.org/10.1016/j.addma.2024.104132.

[14] S. Ghourchian, M. Wyrzykowski, P. Lura, A poromechanics model for plastic shrinkage of fresh cementitious materials, Cem. Concr. Res. 109 (2018) 120–132, http://dx.doi.org/10.1016/j.cemconres.2018.04.013.

[15] X.-Y. Wang, K.-B. Park, Analysis of the compressive strength development of concrete considering the interactions between hydration and drying, Cem. Concr. Res. 102 (2017) 1–15, http://dx.doi.org/10.1016/j.cemconres.2017.08.010.

[16] L. Ma, Q. Zhang, Z. Jia, C. Liu, Z. Deng, Y. Zhang, Effect of drying environment on mechanical properties, internal RH and pore structure of 3D printed concrete, Constr. Build. Mater. 315 (2022) 125731, http://dx.doi.org/10.1016/j.conbuildmat.2021.125731.

[17] T.T. Le, S.A. Austin, S. Lim, R.A. Buswell, R. Law, A.G.F. Gibb, T. Thorpe, Hardened properties of high-performance printing concrete, Cem. Concr. Res. 42 (3) (2012) 558–566, http://dx.doi.org/10.1016/j.cemconres.2011.12.003.

[18] S.C. Paul, Y.W.D. Tay, B. Panda, M.J. Tan, Fresh and hardened properties of 3D printable cementitious materials for building and construction, Arch. Civ. Mech. Eng. 18 (1) (2018) 311–319, http://dx.doi.org/10.1016/j.acme.2017.02.008.

[19] R. Mesnil, V. Poussard, K. Sab, J.-F. Caron, On the geometrical origin of the anisotropy in extrusion-based 3d printed structures, Eng. Struct. 275 (2023) 115082, http://dx.doi.org/10.1016/j.engstruct.2022.115082.

[20] Y. Zhang, Y. Zhang, L. Yang, G. Liu, Y. Chen, S. Yu, H. Du, Hardened properties and durability of large-scale 3D printed cement-based materials, Mater. Struct. 54 (1) (2021) 45, http://dx.doi.org/10.1617/s11527-021-01632-x.

[21] V.N. Nerella, S. Hempel, V. Mechtcherine, Effects of layer-interface properties on mechanical performance of concrete elements produced by extrusion-based 3D-printing, Constr. Build. Mater. 205 (2019) 586–601, http://dx.doi.org/10.1016/j.conbuildmat.2019.01.235.

[22] R.J.M. Wolfs, F.P. Bos, T.A.M. Salet, Hardened properties of 3D printed concrete: The influence of process parameters on interlayer adhesion, Cem. Concr. Res. 119 (2019) 132–140, http://dx.doi.org/10.1016/j.cemconres.2019.02.017.

[23] J.-F. Caron, L. Demont, N. Ducoulombier, R. Mesnil, 3D printing of mortar with continuous fibres: Principle, properties and potential for application, Autom. Constr. 129 (2021) 103806, http://dx.doi.org/10.1016/j.autcon.2021.103806.

[24] F. Bester, J. Kruger, G. van Zijl, Rivet reinforcement for concrete printing, Addit. Manuf. 67 (2023) 103490, http://dx.doi.org/10.1016/j.addma.2023.103490.

[25] H. Liu, C. Liu, Y. Zhang, G. Bai, Bonding properties between 3D printed coarse aggregate concrete and rebar based on interface structural characteristics, Addit. Manuf. 78 (2023) 103893, http://dx.doi.org/10.1016/j.addma.2023.103893.

[26] F.-J. Ulm, O. Coussy, Modeling of thermochemomechanical couplings of concrete at early ages, J. Eng. Mech. 121 (7) (1995) 785–794, http://dx.doi.org/10.1061/(ASCE)0733-9399(1995)121:7(785).

[27] B. Lecampion, A macroscopic poromechanical model of cement hydration, Eur. J. Environ. Civ. Eng. 17 (3) (2013) 176–201, http://dx.doi.org/10.1080/19648189.2013.768554.

[28] N. Agofack, Comportement des ciments pétroliers au jeune âge et intégrité des puits (Ph.D. thesis), Paris Est, 2015.

[29] T. Wangler, Y. Tao, A. Das, M. Mahmoudi, S. Gürel, R.J. Flatt, Aluminate 2K systems in digital concrete: Process, design, chemistry, and outlook, Cem. Concr. Res. 185 (2024) 107644, http://dx.doi.org/10.1016/j.cemconres.2024.107644.

[30] V. Esnault, A. Labyad, M. Chantin, F. Toussaint, Experience in online modification of rheology and strength acquisition of 3D printable mortars, in: T. Wangler, R.J. Flatt (Eds.), First RILEM International Conference on Concrete and Digital Fabrication – Digital Concrete 2018, Springer International Publishing, Cham, 2019, pp. 24–38.

[31] S. Markin, J.A. Cordova, R. Combrinck, V. Mechtcherine, Deformation behaviour of 3D-printed concrete elements induced by plastic shrinkage, Constr. Build. Mater. 449 (2024) 138073, http://dx.doi.org/10.1016/j.conbuildmat.2024.138073.

[32] M. Pierre, M. Samudio, S. Ghabezloo, P. Dangla, Modelling the poromechanical behaviour of class g cement paste: A multiphysics approach from early age to hardened state, Cem. Concr. Res. 193 (2025) 107852, http://dx.doi.org/10.1016/j.cemconres.2025.107852.

[33] H. Darcy, Les Fontaines Publiques De La Ville De Dijon, Victor Dalmont, 1856.

[34] Y. Mualem, A new model for predicting the hydraulic conductivity of unsaturated porous media, Water Resour. Res. 12 (3) (1976) 513–522, http://dx.doi.org/10.1029/WR012i003p00513.

[35] D.W. Taylor, Fundamentals of Soil Mechanics, Wiley, 1948.

[36] V. Picandet, D. Rangeard, A. Perrot, T. Lecompte, Permeability measurement of fresh cement paste, Cem. Concr. Res. 41 (3) (2011) 330–338, http://dx.doi.org/10.1016/j.cemconres.2010.11.019.

[37] S. Gupta, H.S. Esmaeeli, A. Prihar, R.M. Ghantous, W.J. Weiss, R. Moini, Fracture and transport analysis of heterogeneous 3D-printed lamellar cementitious materials, Cem. Concr. Compos. 140 (2023) 105034, http://dx.doi.org/10.1016/j.cemconcomp.2023.105034.

[38] M. Bakhshi, B. Mobasher, C. Soranakom, Moisture loss characteristics of cement-based materials under early-age drying and shrinkage conditions, Constr. Build. Mater. 30 (2012) 413–425, http://dx.doi.org/10.1016/j.conbuildmat.2011.11.015.

[39] P. Coussot, Scaling approach of the convective drying of a porous medium, Eur. Phys. J. B - Condens. Matter Complex Syst. 15 (3) (2000) 557–566, http://dx.doi.org/10.1007/s100510051160.

[40] M. Bakhshi, B. Mobasher, M. Zenouzi, Model for early-age rate of evaporation of cement-based materials, J. Eng. Mech. 138 (11) (2012) 1372–1380, http://dx.doi.org/10.1061/(ASCE)EM.1943-7889.0000435, Publisher: American Society of Civil Engineers.

[41] P. Uno, Plastic shrinkage cracking and evaporation formulas, Aci Mater. J. 95-M34 (1998) 365–375.

[42] I.O. for Standardization, ISO 13788: Hygrothermal performance of building components and building elements — Internal surface temperature to avoid critical surface humidity and interstitial condensation — Calculation methods, 2012.

[43] P. Mounanga, A. Khelidj, G. Bastian, Experimental study and modelling approaches for the thermal conductivity evolution of hydrating cement paste, Adv. Cem. Res. 16 (3) (2004) 95–103, http://dx.doi.org/10.1680/adcr.2004.16.3.95, Publisher: ICE Publishing.

[44] O. Coussy, Poromechanics, second ed., Wiley, 2004.
[45] D.P. Bentz, P.E. Stutzman, F. Zunino, Low-temperature curing strength enhancement in cement-based materials containing limestone powder, Mater. Struct. 50 (3) (2017) 173, http://dx.doi.org/10.1617/s11527-017-1042-6.
[46] M.T. van Genuchten, A closed-form equation for predicting the hydraulic conductivity of unsaturated soils, Soil Sci. Am. J. 44 (5) (1980) 892–898, http://dx.doi.org/10.2136/sssaj1980.03615995004400050002x.
[47] M. Samudio, Modelling of an Oil Well Cement Paste from Early Age to Hardened State : Hydration Kinetics and Poromechanical Behaviour (Ph.D. thesis), Université Paris-Est, 2017.
[48] O. Bernard, F.-J. Ulm, E. Lemarchand, A multiscale micromechanics-hydration model for the early-age elastic properties of cement-based materials, Cem. Concr. Res. 33 (9) (2003) 1293–1309, http://dx.doi.org/10.1016/S0008-8846(03)00039-5.
[49] Eurocode 2: design of concrete structures - part 1-1: general rules and rules for buildings, 2005.
[50] A.C. Institute, ACI CODE-318-19(22): Building code requirements for structural concrete and commentary, 2022.
[51] H. Kada, M. Lachemi, N. Petrov, O. Bonneau, P.C. Aïtcin, Determination of the coefficient of thermal expansion of high performance concrete from initial setting, Mater. Struct. 35 (1) (2002) 35–41, http://dx.doi.org/10.1007/BF02482088.
[52] International Organization for Standardization, ISO 1920-10: Part 10: Determination of static modulus of elasticity in compression, 2012.
[53] R.P. Salvador, S.H. Cavalaro, R. Monte, A.D. de Figueiredo, Relation between chemical processes and mechanical properties of sprayed cementitious matrices containing accelerators, Cem. Concr. Compos. 79 (2017) 117–132, http://dx.doi.org/10.1016/j.cemconcomp.2017.02.002.
[54] I.A. Baratta, J.P. Dean, J.S. Dokken, M. Habera, J. Hale, C.N. Richardson, M.E. Rognes, M.W. Scroggs, N. Sime, G.N. Wells, DOLFINx: The next generation FEniCS problem solving environment, 2023, http://dx.doi.org/10.5281/zenodo.10447666.
[55] T. Helfer, B. Michel, J.-M. Proix, M. Salvo, J. Sercombe, M. Casella, Introducing the open-source mfront code generator: Application to mechanical behaviours and material knowledge management within the PLEIADES fuel element modelling platform, Comput. Math. Appl. 70 (5) (2015) 994–1023, http://dx.doi.org/10.1016/j.camwa.2015.06.027.
[56] J. Bleyer, dolfinx_materials: A Python package for advanced material modelling, 2024, URL https://doi.org/10.5281/zenodo.13882183.
[57] E. Holt, Contribution of mixture design to chemical and autogenous shrinkage of concrete at early ages, Cem. Concr. Res. 35 (3) (2005) 464–472, http://dx.doi.org/10.1016/j.cemconres.2004.05.009.
[58] M. Motamedi, R. Mesnil, A.-M. Tang, J.-M. Pereira, O. Baverel, Structural build-up of 3D printed earth by drying, Addit. Manuf. 95 (2024) 104492, http://dx.doi.org/10.1016/j.addma.2024.104492.
[59] N. Ashrafi, S. Nazarian, N. Meisel, J.P. Duarte, A grammar-based algorithm for toolpath generation: Compensating for material deformation in the additive manufacturing of concrete, Addit. Manuf. 55 (2022) 102803, http://dx.doi.org/10.1016/j.addma.2022.102803.